



# Boron pretreatment promotes phosphorization of FeNi catalysts for oxygen evolution

Chendong Kou<sup>a,b,1</sup>, Jieshu Zhou<sup>a,1</sup>, Haibin Wang<sup>a</sup>, Jingrui Han<sup>a</sup>, Mei Han<sup>a</sup>, Alberto Vomiero<sup>c,d</sup>, Yongchang Liu<sup>a,e</sup>, Hongyan Liang<sup>a,b,\*</sup>

<sup>a</sup> School of Materials Science and Engineering, Tianjin University, Tianjin 300350, PR China

<sup>b</sup> Key Laboratory of Efficient Utilization of Low and Medium Grade Energy, Tianjin University, Tianjin 300350, PR China

<sup>c</sup> Division of Materials Science, Department of Engineering Sciences and Mathematics, Luleå University of Technology, 97187 Luleå, Sweden

<sup>d</sup> Department of Molecular Sciences and Nanosystems, Ca' Foscari University of Venice, Via Torino 155, 30172 Venezia Mestre, Italy

<sup>e</sup> State Key Laboratory of Hydraulic Engineering Simulation and Safety, Tianjin University, Tianjin 300350, PR China

## ARTICLE INFO

### Keywords:

Transition metal phosphide  
NaBH<sub>4</sub> pretreatment  
Self-supported electrode  
Oxygen evolution reaction

## ABSTRACT

Oxygen evolution reaction (OER) is a crucial half-reaction for many energy conversion technologies, which requires efficient catalysts to boost its sluggish kinetics. Herein, the FeNi catalyst with a high phosphating level (HP-Fe<sub>x</sub>Ni<sub>2-x</sub>P) is constructed by a three-step synthetic route: (i) hydrothermal deposition of lamellar sheets, (ii) NaBH<sub>4</sub> pretreatment, and (iii) *in situ* phosphorization. FeNi layered double lamellar hydroxides were synthesized as the pre-catalysts. Then NaBH<sub>4</sub> pretreatment was used to remove the oxide impurities and introduce oxygen vacancies to promote phosphorization in the subsequent process. Finally, HP-Fe<sub>x</sub>Ni<sub>2-x</sub>P nanosheets were achieved, with several advantages like abundant exposed active sites, high conductivity, and accessible mass transport channels. During the OER process, FeNiOOH/HP-Fe<sub>x</sub>Ni<sub>2-x</sub>P interfaces are formed through spontaneous electrochemical activation and surface reconstruction. Benefitting from the synergistic interfacial effect and abundant exposed active sites, the NiFe based catalysts show an overpotential of  $\approx 208$  mV to reach  $10 \text{ mA cm}^{-2}$  in 1 M KOH, and a stability of 200 h at  $1 \text{ A cm}^{-2}$ . Overall, this work reports the rational design and preparation of a highly active OER catalyst, but also provides a general route through NaBH<sub>4</sub> pretreatment, which can be usefully applied to promote phosphorization in other systems of interest for catalytic applications.

## 1. Introduction

Oxygen evolution reaction (OER) is a crucial half-reaction for many energy conversion technologies, such as water splitting [1,2], rechargeable metal-air batteries [3,4], and carbon dioxide reduction [5–7]. However, the high overpotential caused by the sluggish kinetics of OER is a critical bottleneck for efficient energy production and use. Moreover, most commercial catalysts contain noble-metal elements (Ru, Ir, etc.); thus, their high cost, scarcity and poor stability in strong alkaline solutions hinder their industrial applications [8–11]. Therefore, the development of low-cost and earth-abundant transition metal catalysts to counterbalance the present issues of cost, efficiency, and stability is attractive and desirable [12–14].

Transition metal based layered double hydroxides (LDHs) with two-dimensional (2D) structures have attracted increased attention as OER

catalysts since 2013 [15], owing to their numerous advantages, such as high intrinsic OER activity, large surface-to-volume ratio (in comparison with 3D materials), tunable chemical compositions and controllable layered structure adjustments [16]. Unfortunately, LDHs still suffer from deficiencies such as insufficient exposure of active edge sites, high resistance for charge transfer and weak ion transmission rate [16]. Although many design strategies like fabricating nanostructures, combining LDHs with conductive substrates, and creating vacancies, have been tested to alleviate these problems, the functionality of such systems is still inadequate for their industrial exploitation. Recently, many studies have suggested that the catalytic performance of LDHs can be effectively boosted by introducing heteroatoms to form phosphides [17], borides [18,19], or sulfides [20]. Among them, transition metal phosphides (TMPs) have received enormous attention. For example, our recent research found that the phosphorization of NiFeCo can improve

\* Corresponding author at: School of Materials Science and Engineering, Tianjin University, Tianjin 300350, PR China.

E-mail address: [hongyan.liang@tju.edu.cn](mailto:hongyan.liang@tju.edu.cn) (H. Liang).

<sup>1</sup> These authors contributed equally to this work.

the intrinsic catalytic activity and conductivity [21]. The decent OER performance of TMPs can be attributed to several features, such as superior electrical conductivity [22], weakened bonding strength between the metallic bonds [23], and optimized electronic structure [24]. However, despite many studies focusing on TMPs based catalysts, little attention has been paid to the effect of their phosphating level [25,26]. Improving the phosphating level may further enhance the OER performance of phosphides, although relevant studies remain quite limited.

Most TMPs were prepared through a typical phosphating process using  $\text{NaH}_2\text{PO}_2$  as the phosphorus source with high-temperature treatment. The diffusion of metal and phosphorus atoms affects the phosphating level [27]. Therefore, accelerating the diffusion of the atoms is a feasible strategy to facilitate phosphorization. Creating vacancies in crystal lattices may favor atom diffusion and crystal phase transformation [28,29]. Moreover, the coalescence of vacancies can create extra exposed areas, boundaries, or interfaces. Non-hydrogen reduction is a facile way of introducing oxygen vacancies. In recent years,  $\text{NaBH}_4$  modification has been applied in the synthesis of composite materials [30]. For example,  $\text{NaBH}_4$  reduction was used to create oxygen vacancies and defects in LDHs [31,32] or metal oxides [33]. Thus, we hypothesized that introducing  $\text{NaBH}_4$  could break the metal-oxide bonds in LDHs to remove oxygen atoms, providing extra oxygen vacancies, and then facilitating the subsequent phosphorization.

Herein, we presented a new strategy based on hydrothermal growth,  $\text{NaBH}_4$  pretreatment, and *in situ* phosphorization to promote the creation of a new 2D FeNi phosphide composite catalyst with a high phosphating level ( $\text{HP-Fe}_x\text{Ni}_{2-x}\text{P}$ ) on nickel foam (NF). The hydrothermal deposition is used to deposit FeNi LDHs on the surface of NF. Then, the  $\text{NaBH}_4$  pretreatment can reduce the oxides to introduce oxygen vacancies in the FeNi LDHs (denoted as B-FeNi LDHs), resulting in accelerated phosphorization. During the subsequent phosphorization, the B-FeNi LDHs transform into the  $\text{HP-Fe}_x\text{Ni}_{2-x}\text{P}$  nanosheet network, which offers more abundant exposed active sites and higher conductivity compared with the typical  $\text{Fe}_x\text{Ni}_{2-x}\text{P}$  system. During OER, the spontaneously generated  $\text{FeNiOOH}$  layer covered the surface of the  $\text{HP-Fe}_x\text{Ni}_{2-x}\text{P}$ , forming a heterogeneous interface. The  $\text{FeNiOOH/HP-Fe}_x\text{Ni}_{2-x}\text{P}$  heterojunction electrode exhibited an overpotential of  $\approx 208$  mV to reach  $10 \text{ mA cm}^{-2}$  in 1 M KOH and can last for 200 h at  $1 \text{ A cm}^{-2}$ , outperforming the commercial  $\text{RuO}_2/\text{NF}$ . Moreover, the interfacial interaction in  $\text{FeNiOOH/Fe}_x\text{Ni}_{2-x}\text{P}$  and high conductivity contributed to a higher OER activity, as proved by the density functional theory (DFT) calculations, which have rarely been discussed in previous research [34].

## 2. Experimental section

### 2.1. Chemicals

Nickel nitrate hexahydrate ( $\text{Ni}(\text{NO}_3)_2 \cdot 6\text{H}_2\text{O}$ , 98 %), urea ( $\text{CO}(\text{NH}_2)_2$ , 99 %), sodium hydroxide ( $\text{NaOH}$ , 97 %) and Nafion (5 wt%) were purchased from Shanghai Aladdin Reagent Co., Ltd. Ammonium fluoride ( $\text{NH}_4\text{F}$ , AR) and sodium borohydride ( $\text{NaBH}_4$ , AR) were purchased from Tianjin Damao Chemical Reagent Co., Ltd. Potassium hydroxide ( $\text{KOH}$ , 95 %), ferric nitrate nonahydrate ( $\text{Fe}(\text{NO}_3)_3 \cdot 9\text{H}_2\text{O}$ , 98.5 %) and sodium hypophosphite ( $\text{NaH}_2\text{PO}_2$ , 99 %) were purchased from Shanghai Macklin Biochemical Co., Ltd. Hydrochloric acid ( $\text{HCl}$ , AR), nitric acid ( $\text{HNO}_3$ , AR), ethanol absolute (AR) and isopropanol (AR) were purchased from Tianjin Fengchuan Chemical Reagent Technology Co., Ltd. Ruthenium oxide ( $\text{RuO}_2$ , 99.95 %) was purchased from Tianjin Xiensi Biochemical Technology Co., Ltd. NF was purchased from Kunshan Guangjiayuan electronic materials management department. All chemicals were used directly without purification. Milli-Q ultrapure water system manufactured the deionized water in all experiments.

### 2.2. Synthesis of catalysts

**Hydrothermal deposition:** FeNi LDHs were grown on the surface of NF by hydrothermal deposition using a Teflon-lined stainless-steel autoclave. Firstly, the NF ( $3 \text{ cm} \times 5 \text{ cm}$ ) was soaked and sonicated in 3 M  $\text{HCl}$ , deionized water, and ethanol, sequentially. At the same time, the precursor solution was prepared by dissolving 1.2 mmol  $\text{Ni}(\text{NO}_3)_2 \cdot 6\text{H}_2\text{O}$ , 0.6 mmol  $\text{Fe}(\text{NO}_3)_3 \cdot 9\text{H}_2\text{O}$ , 3 mmol  $\text{NH}_4\text{F}$ , and 12 mmol urea in 60 mL deionized water, and kept stirring for 30 min. Afterward, the pretreated NF and the precursor solution were transferred into a 100 mL autoclave and were heated at  $100^\circ\text{C}$  for 7 h. After natural cooling down to room temperature, the NF covered by FeNi LDHs was washed several times with deionized water and ethanol and dried overnight at  $60^\circ\text{C}$  under vacuum conditions. A similar process was used to synthesize  $\text{Ni}(\text{OH})_2$  with  $\text{Ni}(\text{NO}_3)_2 \cdot 6\text{H}_2\text{O}$  as a precursor.

**$\text{NaBH}_4$  pretreatment:** Typically, 0.1 mol  $\text{NaBH}_4$  and 1 mmol  $\text{NaOH}$  were dissolved in 100 mL deionized water and then stirred for 30 min. The FeNi LDHs were soaked in this solution at room temperature for 1 h. After the  $\text{NaBH}_4$  pretreatment, the sample (denoted as B-FeNi LDHs) was dried under vacuum overnight.

***In situ* phosphorization:** The B-FeNi LDHs and 10 mmol  $\text{NaH}_2\text{PO}_2$  were placed into two porcelain boats separately, and the  $\text{NaH}_2\text{PO}_2$  boat was placed upstream of a tubular furnace. Subsequently, the samples were annealed at  $300^\circ\text{C}$  for 2 h with a heating speed of  $1^\circ\text{C min}^{-1}$  under a continuous Ar flow. Finally, the  $\text{HP-Fe}_x\text{Ni}_{2-x}\text{P}$  was collected after cooling down.

### 2.3. Material characterizations

The morphology and elemental distribution and composition of the synthesized catalysts were observed by field emission scanning electron microscopy (SEM, Hitachi S-4800), transmission electron microscopy (TEM, JEM-2100F), energy-dispersive X-ray spectroscopy (EDS), and inductively coupled plasma optical emission spectrometry (ICP-OES). The phase composition and crystallinity of the synthesized catalysts were characterized by powder X-ray diffraction (XRD, Bruker D8) with  $\text{Cu K}\alpha$  radiation. An X-ray photoelectron spectrometer (XPS, Thermo ESCALAB 250XI) was used to analyze the surface chemical states of the synthesized catalysts. The catalysts' evolution during OER was monitored by a Raman spectrometer (Renishaw, in Via microscope). All *in situ* Raman tests were carried out on a three-electrode commercial Raman cell in 0.1 M KOH solution.

### 2.4. Electrochemical measurements

Electrochemical characterizations of these catalysts were conducted on Autolab PGSTAT 302 N electrochemical analyzer with a typical three-electrode system in 1 M KOH ( $\text{pH} = 14$ ) at  $25^\circ\text{C}$ . Self-supporting electrodes synthesized by the above mentioned three-step process ( $0.5 \times 0.5 \text{ cm}^2$ ) were used as the working electrode. The Pt foil was used as the counter electrode, and the  $\text{Ag/AgCl}$  (saturated KCl) electrode was used as the reference electrode. All measured potentials (vs.  $\text{Ag/AgCl}$ ) were converted to the reversible hydrogen electrode (RHE) according to the Nernst equation ( $E_{\text{RHE}} = E_{\text{measured}} + E_{\text{Ag/AgCl}}^0 + 0.0591 \times \text{pH}$ ,  $E_{\text{Ag/AgCl}}^0 = 0.197 \text{ V}$  at  $25^\circ\text{C}$ ,  $\text{pH} = 14$ ). Firstly, 20 cycles of cyclic voltammetry (CV) scans were performed to activate the catalyst. The CV curves were collected from 0 to 1 V (vs.  $\text{Ag/AgCl}$ ) at a scan rate of  $50 \text{ mV s}^{-1}$ . Then the linear sweep voltammetry (LSV) was conducted with a low scan rate of  $1 \text{ mV s}^{-1}$  in the same range. Due to the influence of the Ni oxidation peak, the LSV curves of OER were carried out by negative scanning. The Tafel slope was taken from the linear region of the LSV polarization curve following the Tafel equation:  $\eta = a \times \log j + b$ , where  $\eta$  is the overpotential,  $a$  is the Tafel slope, and  $j$  is the current density. To analyze the reaction kinetics of the catalysts, the electrochemical impedance spectroscopy (EIS) was performed through a CHENHUA electrochemical workstation in the frequency range from 0.01 Hz to 100 kHz with an

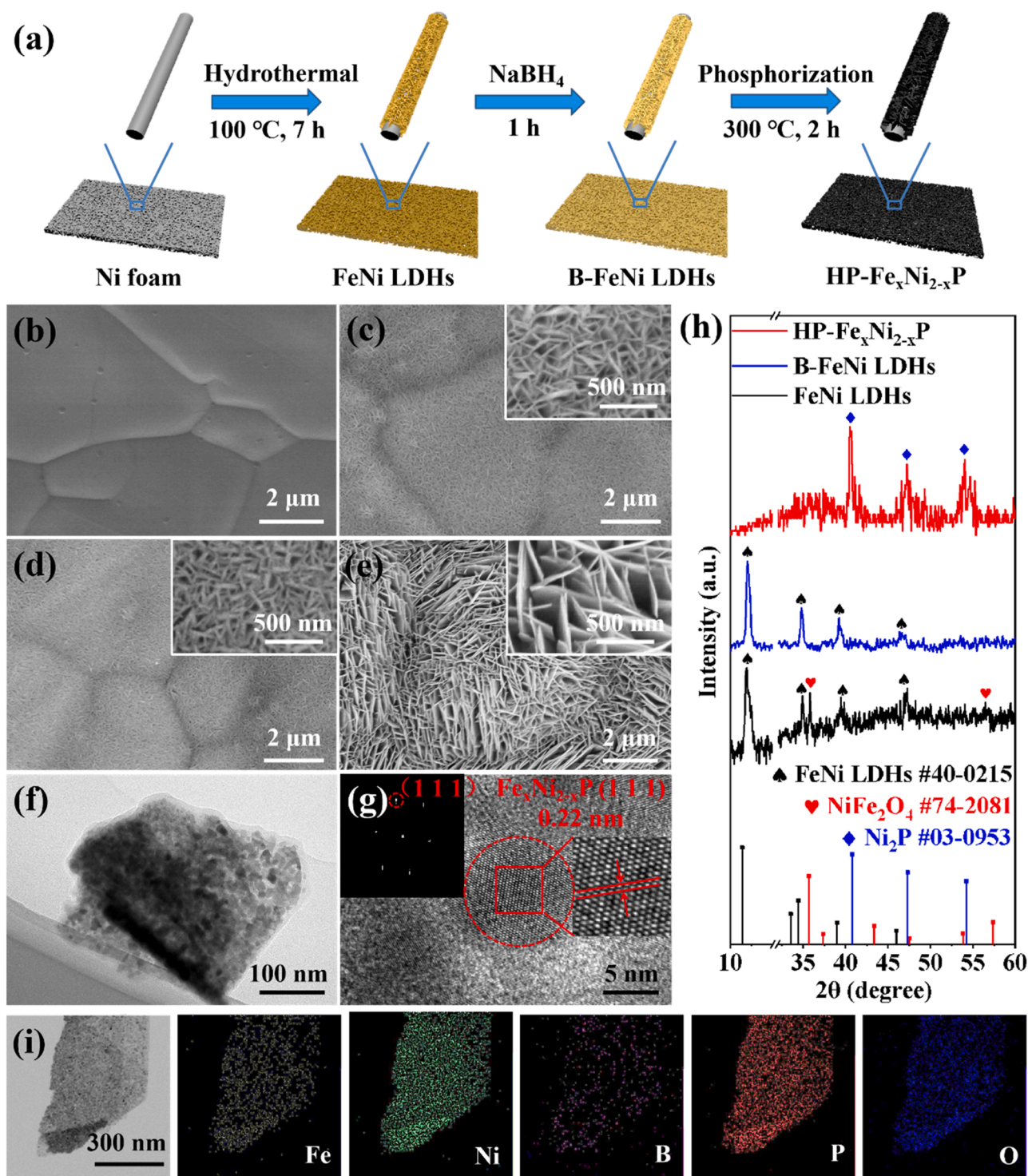


**Fig. 1.** The morphology, structure, and elemental distribution of catalysts. (a) Schematic illustration for the preparation of HP-Fe<sub>x</sub>Ni<sub>2-x</sub>P electrocatalyst, SEM images of (b) NF, (c) FeNi LDHs, (d) B-FeNi LDHs and (e) HP-Fe<sub>x</sub>Ni<sub>2-x</sub>P electrocatalysts, (f) TEM and (g) HRTEM image of HP-Fe<sub>x</sub>Ni<sub>2-x</sub>P electrocatalyst, (h) XRD patterns of FeNi LDHs, B-FeNi LDHs and HP-Fe<sub>x</sub>Ni<sub>2-x</sub>P electrocatalysts, (i) TEM-EDS elemental mapping images of HP-Fe<sub>x</sub>Ni<sub>2-x</sub>P electrocatalyst.

amplitude of 5 mV at an overpotential of 240 mV [35]. The electrochemical active surface area (ECSA) and double-layer capacitance ( $C_{dl}$ ) were obtained by CV scans in the non-Faradic region at various scan rates from 20 to 120 mV s<sup>-1</sup> [31,36]. The stability of the catalyst was measured by chronopotentiometry at a current density of 1 A cm<sup>-2</sup>. All electrochemical data were handled with the 85 %  $iR$  correction without additional notes, where  $R$  is the solution resistance ( $R_s$ ) mentioned in the impedance data.

To prepare the commercial RuO<sub>2</sub> working electrode, 10 mg RuO<sub>2</sub> powder was dispersed in a mixture containing 650  $\mu$ L water, 330  $\mu$ L isopropanol, and 20  $\mu$ L Nafion solution. After that, the as-prepared suspension was continuously sonicated for at least 30 min. Finally, 100  $\mu$ L catalyst ink was transferred to the NF with an exposed working area of  $0.5 \times 0.5$  cm<sup>2</sup> and dried overnight at room temperature.



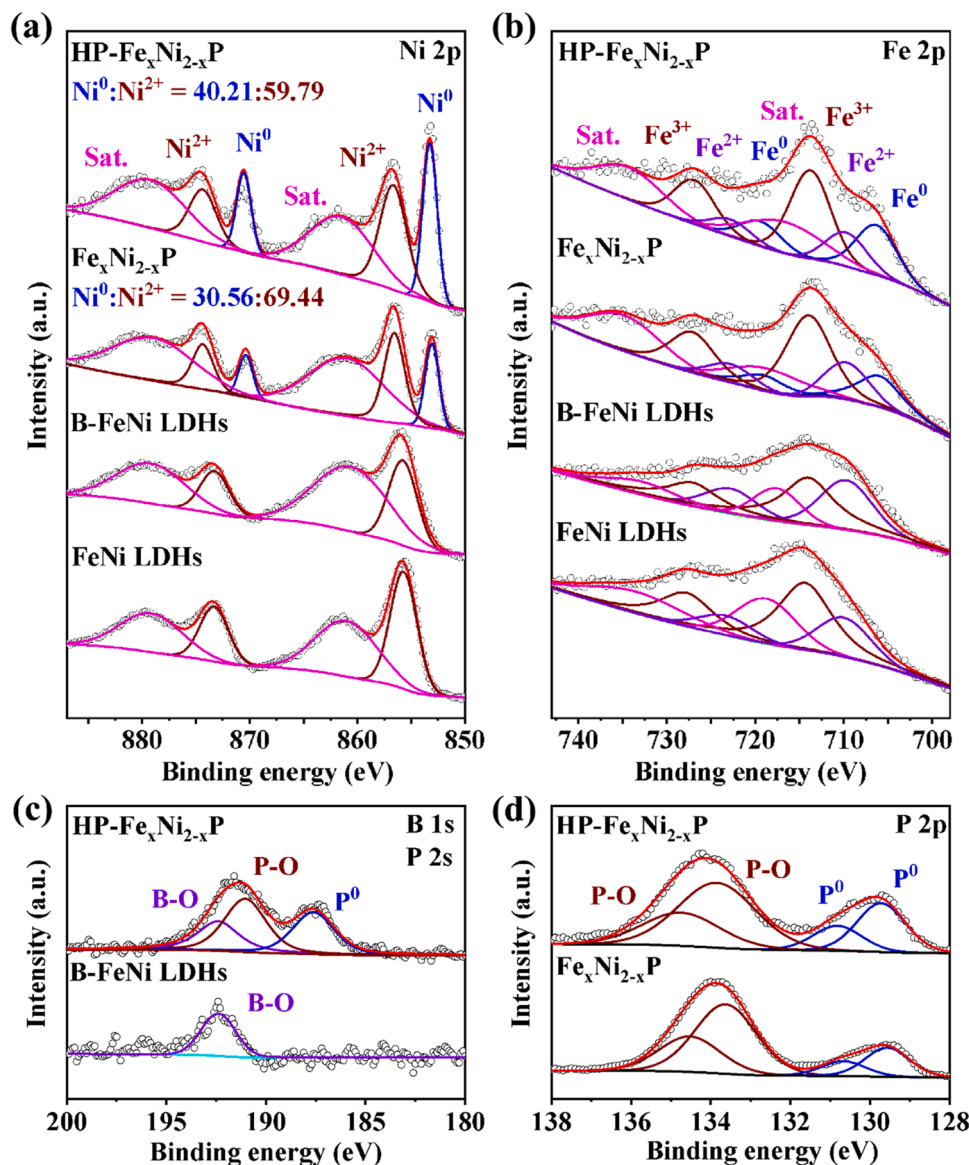
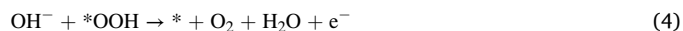


Fig. 2. The XPS spectra. (a) Ni 2p and (b) Fe 2p of FeNi LDHs, B-FeNi LDHs,  $\text{Fe}_x\text{Ni}_{2-x}\text{P}$  and  $\text{HP-Fe}_x\text{Ni}_{2-x}\text{P}$  electrocatalysts, (c) B 1s and P 2s of B-FeNi LDHs and  $\text{HP-Fe}_x\text{Ni}_{2-x}\text{P}$  electrocatalysts, (d) P 2p of  $\text{Fe}_x\text{Ni}_{2-x}\text{P}$  and  $\text{HP-Fe}_x\text{Ni}_{2-x}\text{P}$  electrocatalysts.

## 2.5. Computational methods

DFT calculations with a plane-wave basis were performed as implemented in Vienna *ab initio* Simulation Package (VASP) [37]. Projector augmented wave (PAW) pseudopotentials were used. The exchange-correlation contributions to the total energy were estimated by the generalized gradient approximation (GGA) with Perdew-Burke-Ernzerhof (PBE) form [38]. For a better description of the Ni and Fe 3d electrons, the Hubbard effective terms  $U_{\text{eff}}(\text{Ni}) = 5.5$  eV and  $U_{\text{eff}}(\text{Fe}) = 3.5$  eV were added to the PBE functional [39]. A kinetic-energy cutoff of 450 eV was used. During geometry optimizations, the maximum force on each atom was less than  $0.05$  eV  $\text{\AA}^{-1}$ . The total energy convergence criterion was set as  $10^{-5}$  eV. Spin polarization was considered in all calculations. We used a deprotonating  $\beta$ -FeNiOOH structure to represent  $\gamma$ -FeNiOOH. The heterojunction of  $\gamma$ -FeNiOOH (0 1  $\bar{1}$  2)/ $\text{Fe}_x\text{Ni}_{2-x}\text{P}$  (1 1 1) were built, where the vacuum space along the z direction is set to be  $15$   $\text{\AA}$ , which is enough to avoid interaction between the two neighboring images [40]. The Brillouin zone was sampled by k-point meshes of  $2 \times 2 \times 1$ . For structural relaxation, the bottom atomic layer was fixed, and all other atoms and adsorbates were fully

relaxed. The OER under alkaline conditions consists of four elementary reaction steps, each involving an electron transfer to the electrode.



To express the thermochemistry of the sub-reactions of OER, the computational hydrogen electrode (CHE) model proposed by Nørskov et al. was used [41]. The reaction free energy change of each step was calculated using the following equation:

$$\Delta G_i = \Delta E_i + \Delta \text{ZPE}_i - T \Delta S_i \quad (5)$$

where  $i = 1, 2, 3, 4$ , corresponds to each step in OER.  $\Delta E$  is the reaction energy,  $\Delta \text{ZPE}$  is the change of zero-point energy,  $T$  (298.15 K) is temperature,  $\Delta S$  is the difference in entropy.



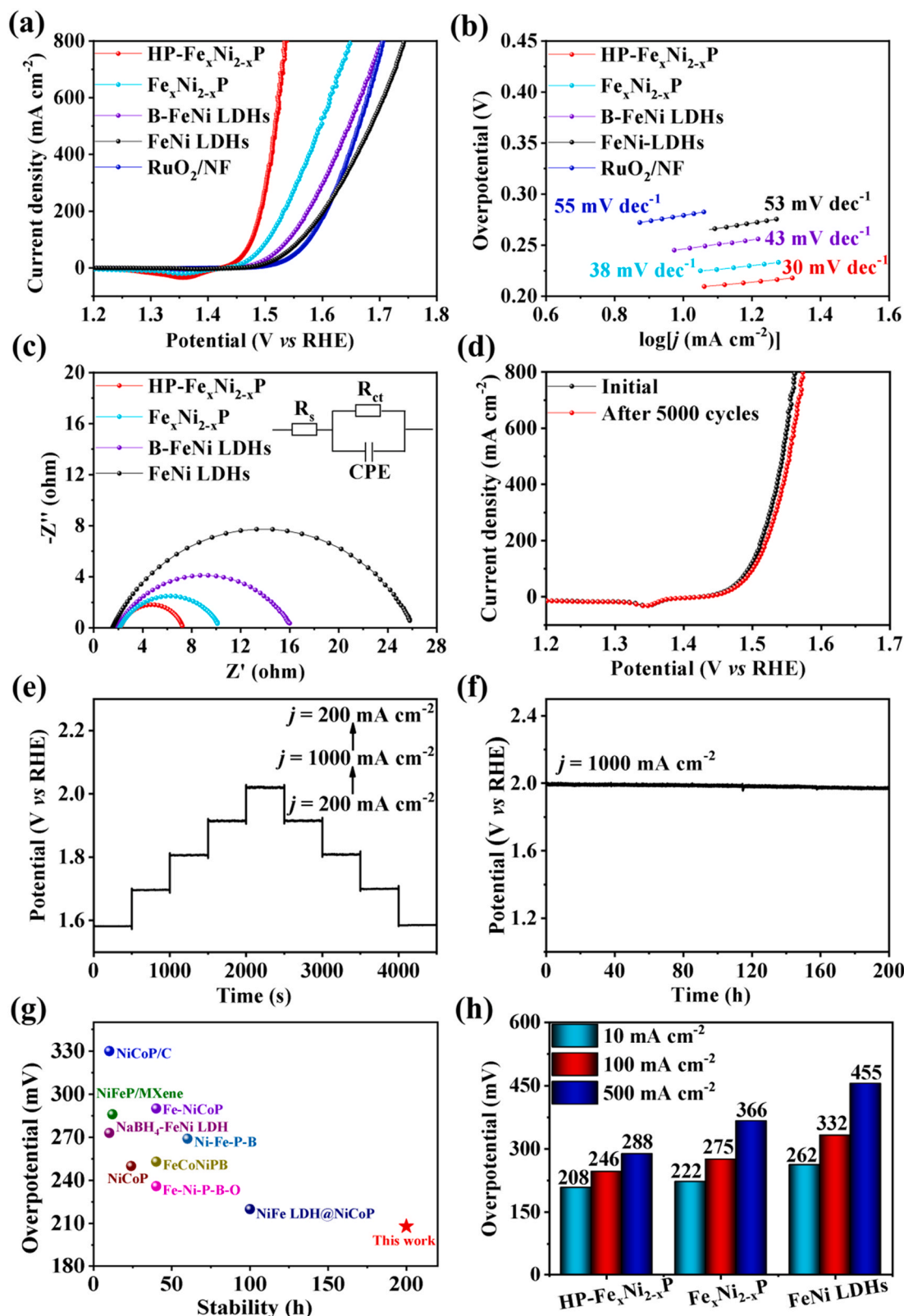


**Fig. 3.** The characterizations for electrocatalytic OER performance. (a) LSV curves, (b) Tafel plots of FeNi LDHs, B-FeNi LDHs, Fe<sub>x</sub>Ni<sub>2-x</sub>P, HP-Fe<sub>x</sub>Ni<sub>2-x</sub>P and RuO<sub>2</sub> electrocatalysts in 1 M KOH, (c) Nyquist plots of FeNi LDHs, B-FeNi LDHs, Fe<sub>x</sub>Ni<sub>2-x</sub>P and HP-Fe<sub>x</sub>Ni<sub>2-x</sub>P electrocatalysts in 1 M KOH, (d) LSV curves of HP-Fe<sub>x</sub>Ni<sub>2-x</sub>P before and after 5000 CV cycles in 1 M KOH, (e) multiple current steps of chronopotentiometry experiment for HP-Fe<sub>x</sub>Ni<sub>2-x</sub>P electrocatalyst, the current density started at 200 mA cm<sup>-2</sup> and finished at 1000 mA cm<sup>-2</sup>, with an increment of 200 mA cm<sup>-2</sup> per 500 s, then dropped to 200 mA cm<sup>-2</sup> with the same rule without *iR* correction, (f) chronopotentiometry at a current density of 1000 mA cm<sup>-2</sup> in 1 M KOH without *iR* correction, (g) comparison of performance with other similar work, (h) overpotential at the current density of 10 mA cm<sup>-2</sup>, 100 mA cm<sup>-2</sup> and 500 mA cm<sup>-2</sup>.

### 3. Results and discussion

#### 3.1. Characterizations of synthesized pre-catalysts

Typically, self-supported HP-Fe<sub>x</sub>Ni<sub>2-x</sub>P nanosheet arrays on NF were prepared by a three-step synthesis, the hydrothermal deposition, the NaBH<sub>4</sub> pretreatment, and the *in situ* phosphorization [21,42], as shown in Fig. 1a. NF was used as the substrate because it provides a large surface area and a high conductivity. The morphological, structural, and compositional features of the as-prepared materials were characterized. Fig. 1b–c shows that after the hydrothermal deposition at 100 °C for 7 h, a layer of 500-nm-thick (Fig. S1a) dense nanosheet arrays grew on the smooth surface of NF. Their XRD pattern (Fig. 1h) shows sharp diffraction peaks at 11.6°, 34.6°, 39.2°, and 46.4°, which can be ascribed to (0 0 3), (0 1 2), (0 1 5), and (0 1 8) reflections from FeNi LDHs (PDF# 40-0215), respectively [26,43,44]. In addition, the diffraction peaks at 35.9° and 57.2° are assigned to (3 1 1) and (5 1 1) planes of NiFe<sub>2</sub>O<sub>4</sub> (PDF# 74-2081) [45], indicating the appearance of oxide impurities in FeNi LDHs. After the NaBH<sub>4</sub> pretreatment, the XRD peaks of oxide impurities disappeared. However, the morphology and crystal structure of FeNi LDHs did not change significantly, except for the formation of a surface amorphous layer (Fig. 1d, h and Fig. S1b–d) [31]. The possible reason is that the reductant NaBH<sub>4</sub> works as an oxygen scavenger to reduce oxide impurities, resulting in an amorphized surface structure with abundant vacancies.

*In situ* phosphating treatment was carried out at 300 °C for 2 h. B-FeNi LDHs transformed into HP-Fe<sub>x</sub>Ni<sub>2-x</sub>P, and denser nanosheet arrays were achieved (Fig. 1e). The XRD diffraction pattern (Fig. 1h) of the HP-Fe<sub>x</sub>Ni<sub>2-x</sub>P shows peaks at about 40.6°, 47.3° and 54.2° corresponding to the (1 1 1), (2 1 0) and (3 0 0) planes of Ni<sub>2</sub>P (PDF#03-0953), respectively. However, compared with the pure Ni<sub>2</sub>P, the lattice constants of HP-Fe<sub>x</sub>Ni<sub>2-x</sub>P increased, and the diffraction peak of the (1 1 1) plane was offset by about 0.2° towards the small angle direction (Fig. S2). The expansion of lattice distance might be caused by Fe substitution, which has a larger atomic radius than that of Ni [46]. In addition, we did not find the signal of FeNi LDHs in the XRD pattern of HP-Fe<sub>x</sub>Ni<sub>2-x</sub>P, indicating no existence of the crystalline FeNi LDHs structure (Fig. 1h). Then, the morphology and structure of HP-Fe<sub>x</sub>Ni<sub>2-x</sub>P were further characterized by TEM and HRTEM (Fig. 1f–g and Fig. S3), which revealed that Fe<sub>x</sub>Ni<sub>2-x</sub>P crystalline nanoparticles are dispersed in an amorphous nanosheet. Moreover, elemental mapping in HP-Fe<sub>x</sub>Ni<sub>2-x</sub>P confirmed the existence of uniformly dispersed Fe and Ni, as well as B and P elements (Fig. 1i). The elemental mapping and EDS spectrum of Fe<sub>x</sub>Ni<sub>2-x</sub>P (without NaBH<sub>4</sub> pretreatment, Fig. S4) were compared with that of HP-Fe<sub>x</sub>Ni<sub>2-x</sub>P. The results show that the atomic percentage of P in HP-Fe<sub>x</sub>Ni<sub>2-x</sub>P is higher than that in Fe<sub>x</sub>Ni<sub>2-x</sub>P, indicating that the NaBH<sub>4</sub> pretreatment process could improve the level of phosphorization. Pure Ni<sub>2</sub>P was fabricated as a control sample, and the related TEM and HRTEM images in Fig. S5 confirmed its crystalline structure.

Raman spectra were also used to investigate the pre-catalysts. As shown in Fig. S6, the control sample Ni(OH)<sub>2</sub> shows one peak at around 466 cm<sup>-1</sup>, which is attributed to the vibrations of Ni<sup>II</sup>-O in Ni(OH)<sub>2</sub> crystal [47]. After hydrothermal deposition, the FeNi LDHs were achieved, which exhibited peaks at around 466 and 534 cm<sup>-1</sup> corresponding to the vibrations of Ni<sup>II</sup>-O in Ni(OH)<sub>2</sub> crystal and defective or disordered Ni(OH)<sub>2</sub> [47–50], respectively. The peaks located at around 313 cm<sup>-1</sup> and 725 cm<sup>-1</sup> can be ascribed to E<sub>g</sub> and A<sub>1g</sub> Raman bands in the NiFe<sub>2</sub>O<sub>4</sub> impurities [49,51]. After NaBH<sub>4</sub> pretreatment, the peak intensities of NiFe<sub>2</sub>O<sub>4</sub> impurities decreased dramatically, which means that the oxide structure was destroyed, consistently with the XRD results. After *in situ* phosphating treatment, the Raman features of LDHs disappeared due to the phase transformation from LDHs to phosphide [52,53].

To study the valence states of the elements in these catalysts, XPS was performed. The survey XPS spectra in Fig. S7 revealed the coexistence of various elements in the pre-catalysts. The high-resolution Ni 2p

spectra in FeNi LDHs in Fig. 2a exhibited two main characteristic peaks at 855.8 and 873.1 eV, which could be attributed to Ni<sup>2+</sup> 2p<sub>3/2</sub> and Ni<sup>2+</sup> 2p<sub>1/2</sub> respectively [26,43,54,55]. The high-resolution Fe 2p spectra of FeNi LDHs in Fig. 2b show four main characteristic peaks at 709.7, 722.8, 713.7, and 726.8 eV, attributed to Fe<sup>2+</sup> 2p<sub>3/2</sub>, Fe<sup>2+</sup> 2p<sub>1/2</sub>, Fe<sup>3+</sup> 2p<sub>3/2</sub>, and Fe<sup>3+</sup> 2p<sub>1/2</sub> respectively [32,56]. The signal of Fe<sup>3+</sup> can be attributed to the NiFe<sub>2</sub>O<sub>4</sub> impurities and the surface oxides.

After NaBH<sub>4</sub> pretreatment, the valence states of Fe and Ni in B-FeNi LDHs catalyst are still Fe<sup>2+</sup>, Fe<sup>3+</sup>, and Ni<sup>2+</sup>, and the B-O peak appears at 192.4 eV (Fig. 2c) [22,31,57,58]. The ratio of Fe<sup>2+</sup>/Fe<sup>3+</sup> increases from 0.45 for NiFe LDHs to 0.78 for the B-FeNi LDHs, because NaBH<sub>4</sub> reduced the high valent Fe oxides. Moreover, the high-resolution O 1s spectra in Fig. S8 exhibit four peaks located at 529.7, 531.0, 531.6, and 533.1 eV, which are assigned to O-M, O-H, oxygen vacancies (O<sub>v</sub>), and adsorbed water (H<sub>2</sub>O), respectively. Obviously, the peak area of O<sub>v</sub> in B-FeNi LDHs is larger, indicating a high content of oxygen vacancies [32].

Then, after *in situ* phosphating treatment, two pairs of peaks appeared in the high-resolution XPS of Ni 2p at 853.3 and 870.6 eV, related to the Ni<sup>0</sup> 2p<sub>3/2</sub> and Ni<sup>0</sup> 2p<sub>1/2</sub>, and at 706.3 and 719.4 eV, related to the Fe<sup>0</sup> 2p<sub>3/2</sub> and Fe<sup>0</sup> 2p<sub>1/2</sub> (Fig. 2a) and Fe 2p (Fig. 2b) in HP-Fe<sub>x</sub>Ni<sub>2-x</sub>P catalyst. The high-resolution XPS of P 2s and B 1s in HP-Fe<sub>x</sub>Ni<sub>2-x</sub>P can be deconvoluted into three characteristic peaks, where the peaks at 187.6 and 191.1 eV correspond to P<sup>0</sup> and P-O, and the peak at 192.4 eV can be ascribed to B-O (Fig. 2c). In the high-resolution XPS spectrum of P 2p in HP-Fe<sub>x</sub>Ni<sub>2-x</sub>P four characteristic peaks can be identified, where the peaks at 129.8 and 130.7 eV are corresponding to P<sup>0</sup> 2p<sub>3/2</sub> and P<sup>0</sup> 2p<sub>1/2</sub>, and the peaks at 133.9 and 134.8 eV can be ascribed to P-O (Fig. 2d) [42,59,60]. The appearance of Ni<sup>0</sup>, Fe<sup>0</sup>, and P<sup>0</sup> in XPS indicated that FeNi LDHs were converted to the Fe<sub>x</sub>Ni<sub>2-x</sub>P phase after the phosphating process. This conclusion is consistent with XRD and TEM analyses. Compared with the control sample without NaBH<sub>4</sub> pretreatment, the Ni<sup>0</sup>/Ni<sup>2+</sup> ratio is higher in HP-Fe<sub>x</sub>Ni<sub>2-x</sub>P. The possible reason is that the NaBH<sub>4</sub> pretreatment removes the surface oxides and promotes partial surface amorphization, which facilitates the subsequent phosphating treatment.

#### 3.2. Electrocatalytic performance for OER

The electrocatalytic performance of HP-Fe<sub>x</sub>Ni<sub>2-x</sub>P catalyst for OER was evaluated on a conventional three-electrode system under alkaline pH conditions of 1 M KOH (pH = 14) at 25 °C. Before electrocatalytic evaluation, 20 cycles of CV scans were performed for electrochemical pre-activation. As a control, Fe<sub>x</sub>Ni<sub>2-x</sub>P, B-FeNi LDHs, FeNi LDHs, and commercial RuO<sub>2</sub>/NF were measured under the same condition.

The HP-Fe<sub>x</sub>Ni<sub>2-x</sub>P electrode requires the lowest overpotential (≈ 208 mV) to reach 10 mA cm<sup>-2</sup> compared to the other electrodes, which is superior to the performance of the commercial RuO<sub>2</sub>/NF electrode. To show the performance difference between HP-Fe<sub>x</sub>Ni<sub>2-x</sub>P, Fe<sub>x</sub>Ni<sub>2-x</sub>P, and FeNi LDHs catalysts more intuitively, the histogram of overpotential at the current density of 10 mA cm<sup>-2</sup>, 100 mA cm<sup>-2</sup>, and 500 mA cm<sup>-2</sup> is reported in Fig. 3h. A detailed comparison of different OER catalysts is listed in Table S1 and Fig. 3g, further verifying the outstanding OER activity of HP-Fe<sub>x</sub>Ni<sub>2-x</sub>P electrode. To gain further insight into the HP-Fe<sub>x</sub>Ni<sub>2-x</sub>P electrode, the corresponding Tafel plots were compared to explain the OER kinetics (Fig. 3b). OER is related to electrochemical kinetics: the smaller the slope in the Tafel plot, the faster the reaction speed is. The Tafel slopes of HP-Fe<sub>x</sub>Ni<sub>2-x</sub>P, Fe<sub>x</sub>Ni<sub>2-x</sub>P, B-FeNi LDHs, FeNi LDHs, and commercial RuO<sub>2</sub>/NF were 30 mV dec<sup>-1</sup>, 38 mV dec<sup>-1</sup>, 43 mV dec<sup>-1</sup>, 53 mV dec<sup>-1</sup>, and 55 mV dec<sup>-1</sup>, respectively, indicating the fastest OER rates of HP-Fe<sub>x</sub>Ni<sub>2-x</sub>P electrode. EIS at a constant overpotential of 240 mV was further applied to probe the electrode kinetics under the OER process. As shown in Fig. 3c, the Nyquist plots in the high-frequency range present standard semicircles, whose diameters are determined by the charge-transfer resistance (R<sub>ct</sub>). The R<sub>ct</sub> of HP-Fe<sub>x</sub>Ni<sub>2-x</sub>P is about 5.12 Ω, which is much smaller than those of Fe<sub>x</sub>Ni<sub>2-x</sub>P (≈ 7.97 Ω), B-FeNi LDHs (≈ 14.09 Ω), and FeNi

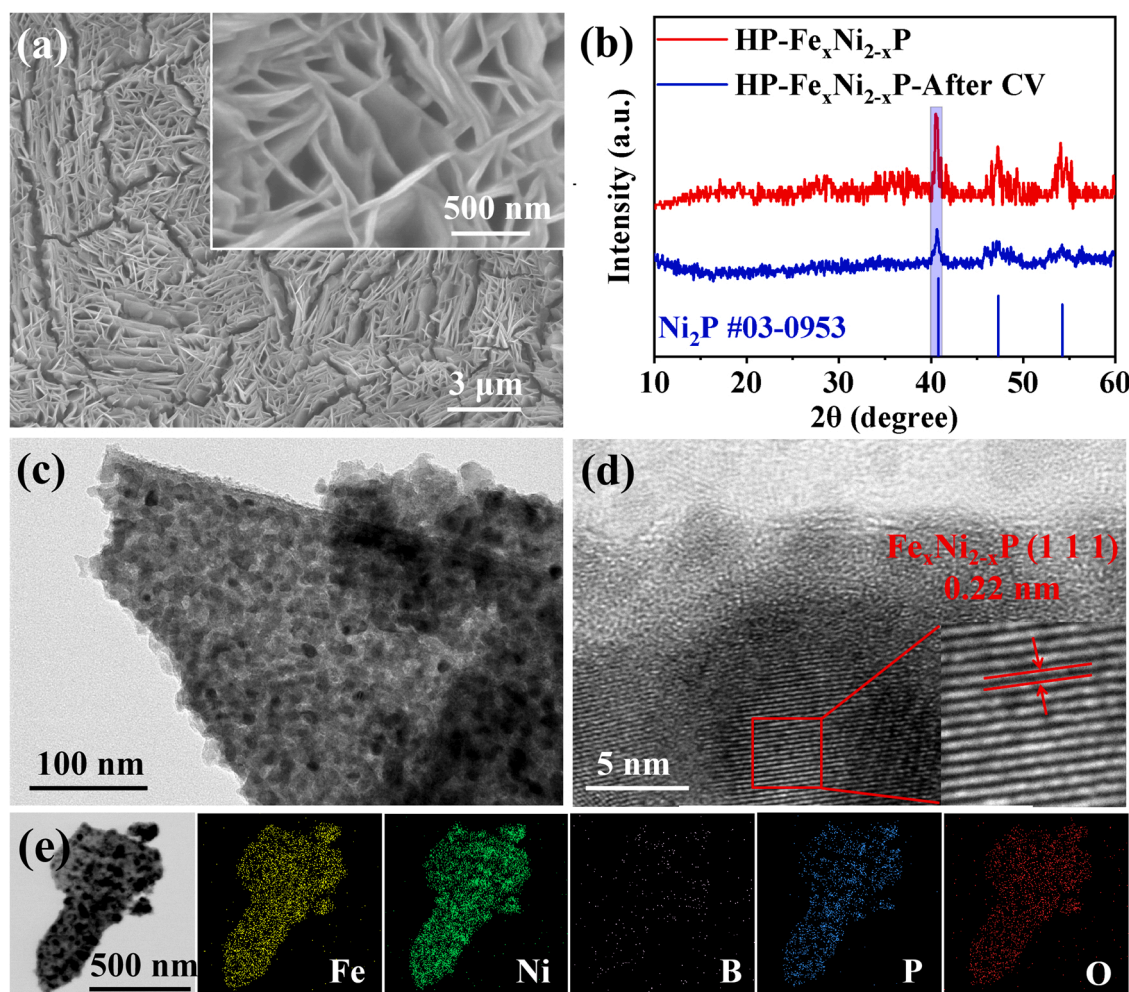


**Fig. 4.** The morphology, crystal structure and elemental distribution of HP-Fe<sub>x</sub>Ni<sub>2-x</sub>P catalyst after 20 cycles of CV. (a) SEM, (b) XRD, (c) TEM, (d) HRTEM images and (e) TEM-EDS elemental mapping images.

LDHs ( $\approx 24.60 \Omega$ ), suggesting a rapid charge transfer rate in the HP-Fe<sub>x</sub>Ni<sub>2-x</sub>P catalyst [21,26]. In addition, we can conclude that  $R_s$  is about  $2.0 \Omega$  from the intersection of the curve and the abscissa, which can be used for  $iR$  correction. We analyzed the CV curves of HP-Fe<sub>x</sub>Ni<sub>2-x</sub>P, Fe<sub>x</sub>Ni<sub>2-x</sub>P, and FeNi LDHs catalysts without  $iR$  correction (Fig. S9). Compared with FeNi LDHs catalyst, there is a large oxidation current of phosphide during the first cycle of CV in the HP-Fe<sub>x</sub>Ni<sub>2-x</sub>P and Fe<sub>x</sub>Ni<sub>2-x</sub>P catalysts. The phenomenon of the oxidation current in HP-Fe<sub>x</sub>Ni<sub>2-x</sub>P is larger than in Fe<sub>x</sub>Ni<sub>2-x</sub>P, further indicating that NaBH<sub>4</sub> pretreatment is beneficial to phosphatization.

We further evaluated the ECSA of as-prepared catalysts to understand the intrinsic surface-area activity, which is proportional to the  $C_{dl}$  shown in Fig. S10a. HP-Fe<sub>x</sub>Ni<sub>2-x</sub>P possess a  $C_{dl}$  value of  $5.79 \text{ mF cm}^{-2}$ , which is larger than that for Fe<sub>x</sub>Ni<sub>2-x</sub>P ( $4.51 \text{ mF cm}^{-2}$ ), B-FeNi LDHs ( $2.61 \text{ mF cm}^{-2}$ ) and FeNi LDHs ( $2.16 \text{ mF cm}^{-2}$ ). The CV curves of as-prepared catalysts at different scan rates of 20, 40, 60, 80, 100, and  $120 \text{ mV s}^{-1}$  in a non-Faradaic region are shown in Fig. S10c–f. ECSA values were then calculated to be 145, 113, 65, and 54 for HP-Fe<sub>x</sub>Ni<sub>2-x</sub>P, Fe<sub>x</sub>Ni<sub>2-x</sub>P, B-FeNi LDHs, and FeNi LDHs, respectively. This shows that the phosphating process can increase the ECSA value, and increasing the level of phosphorization is beneficial to further increase the number of exposed active sites. We further normalized current density by the ECSA (Fig. S10b): HP-Fe<sub>x</sub>Ni<sub>2-x</sub>P has the highest normalized OER activity, indicating that, after excluding the effect of the active surface area, the HP-Fe<sub>x</sub>Ni<sub>2-x</sub>P sample exhibits the highest intrinsic catalytic activity among all the catalysts.

OER electrochemical stability is another critical factor in evaluating catalysts' performance. Fig. 3d shows LSV curves of HP-Fe<sub>x</sub>Ni<sub>2-x</sub>P before and after 5000 CV cycles in 1 M KOH to demonstrate the cyclic stability of the catalyst. We can see that the OER performance of the sample does not change after CV cycles. Fig. 3e shows the multiple current steps of the chronopotentiometry experiment for the HP-Fe<sub>x</sub>Ni<sub>2-x</sub>P electrocatalyst. When the current density increased from  $200 \text{ mA cm}^{-2}$  to  $1000 \text{ mA cm}^{-2}$  and then dropped to  $200 \text{ mA cm}^{-2}$ , the curves remained constant for at least 500 s, proving the excellent step stability of the sample. Furthermore, the long-term OER process stability test was carried out for 200 h at a fixed current density of  $1000 \text{ mA cm}^{-2}$  (Fig. 3f), and there was no evident voltage increase. In conclusion, the HP-Fe<sub>x</sub>Ni<sub>2-x</sub>P catalyst has excellent OER stability in 1 M KOH.

### 3.3. OER mechanism investigation

To further study the overall modification of the catalyst during OER, the HP-Fe<sub>x</sub>Ni<sub>2-x</sub>P catalyst after 20 cycles of CV was examined by SEM, XRD, TEM, HRTEM, and EDS. The SEM image (Fig. 4a) shows that the morphology of HP-Fe<sub>x</sub>Ni<sub>2-x</sub>P nanosheet arrays was retained without noticeable change. Fig. 4b shows that the diffraction peak of Fe<sub>x</sub>Ni<sub>2-x</sub>P became weak after the reaction, indicating that the phosphide was partially oxidized. The TEM and HRTEM images (Fig. 4c–d) indicate that, after OER, the crystalline Fe<sub>x</sub>Ni<sub>2-x</sub>P particles are still separately dispersed without obvious agglomeration [26]. In addition, a thin



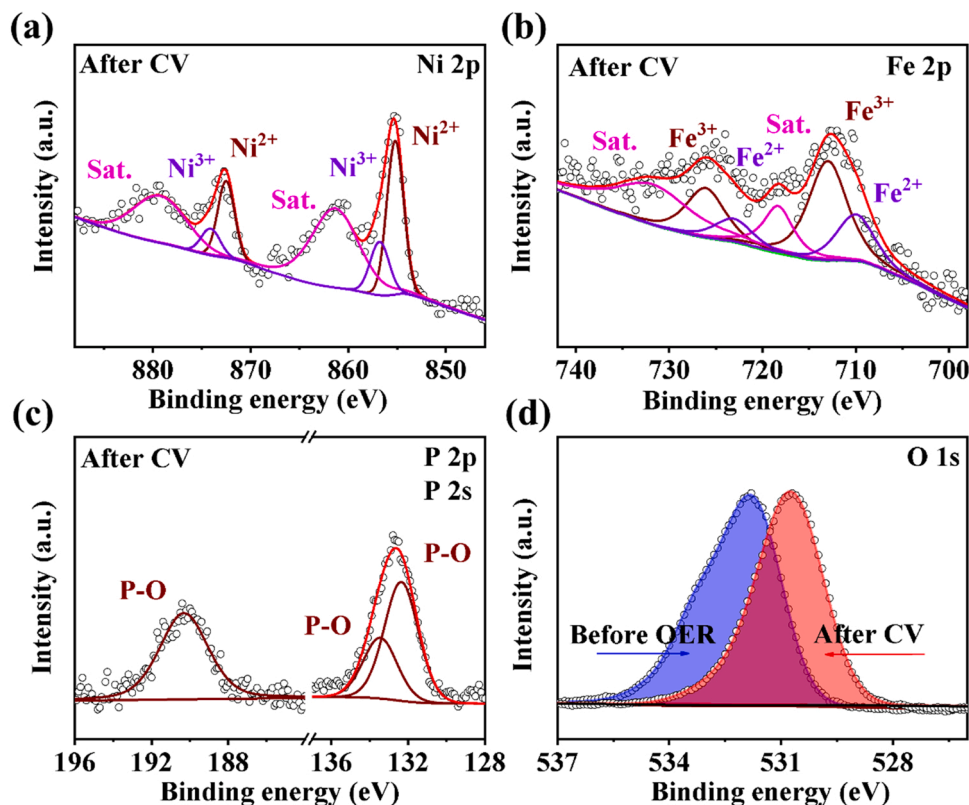


Fig. 5. The XPS spectra. The high resolution XPS spectra of (a) Ni 2p, (b) Fe 2p, (c) P 2p, P 2s of HP-Fe<sub>x</sub>Ni<sub>2-x</sub>P electrocatalyst after 20 cycles of CV, and (d) O 1s of HP-Fe<sub>x</sub>Ni<sub>2-x</sub>P electrocatalysts before and after 20 cycles of CV.

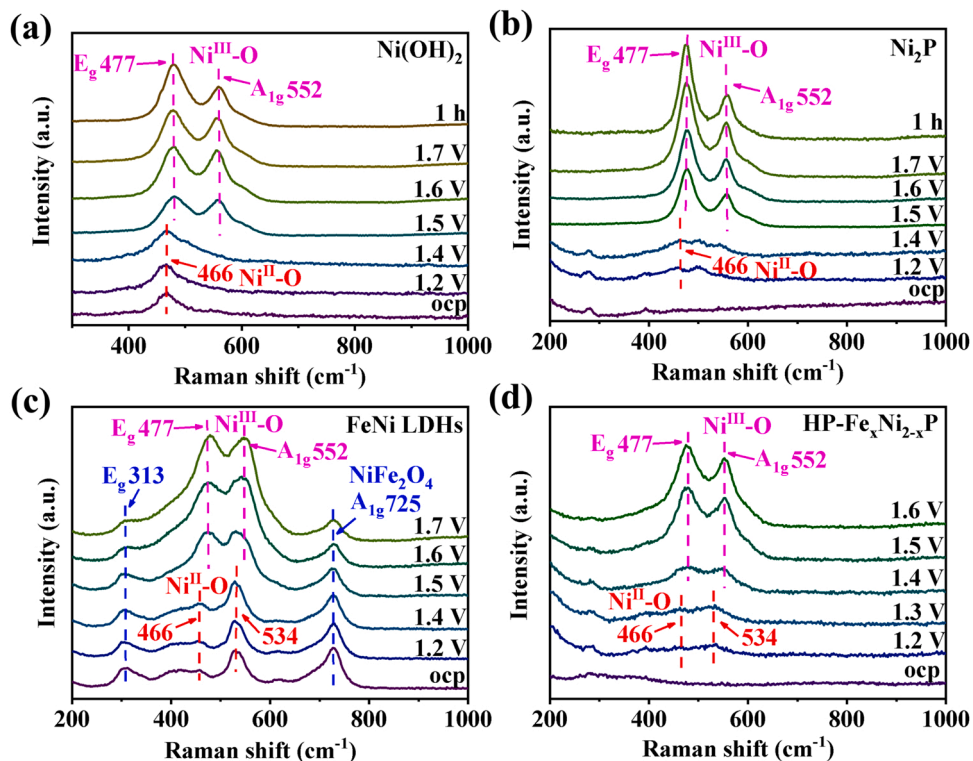
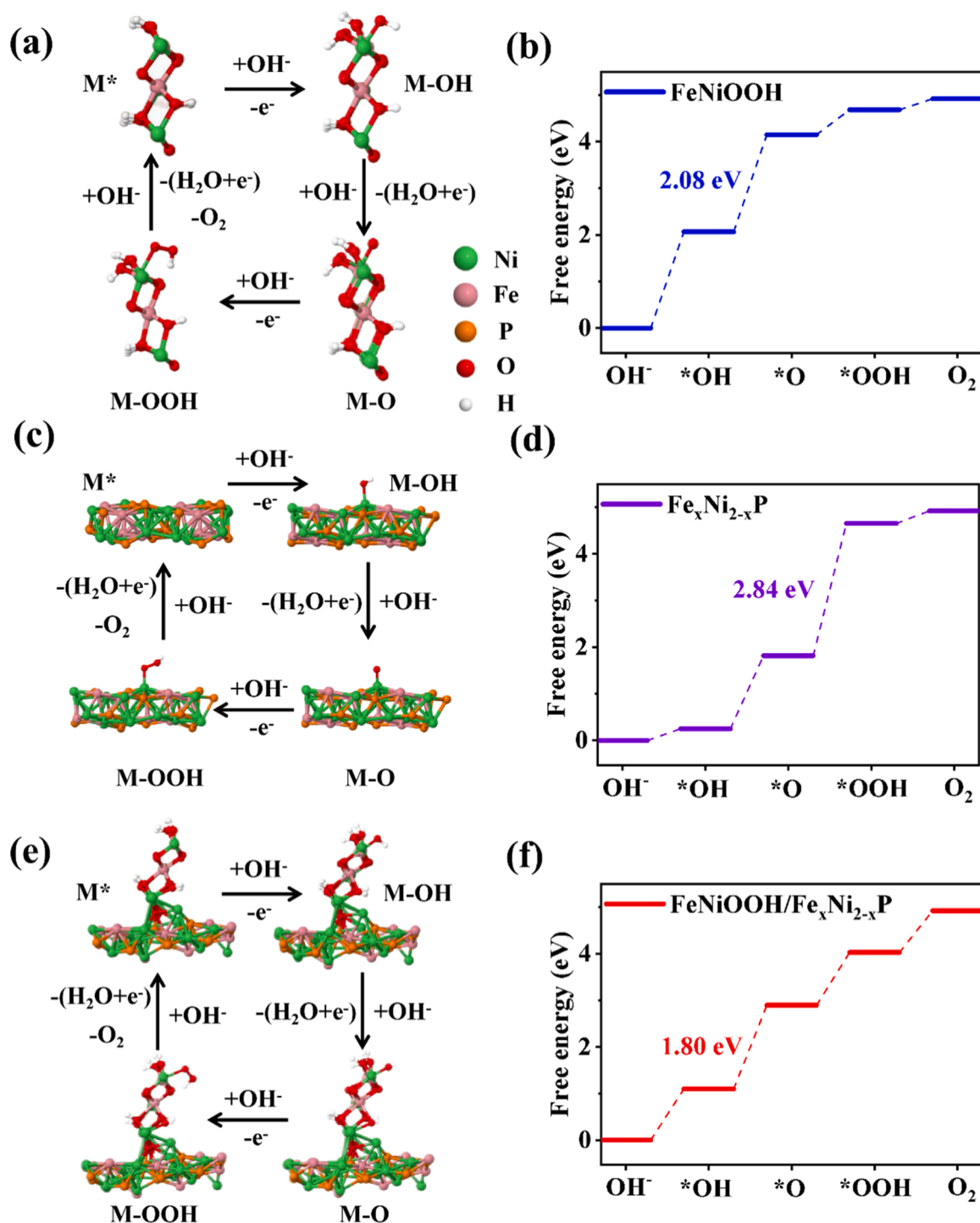


Fig. 6. In situ Raman spectra of (a) Ni(OH)<sub>2</sub>, (b) Ni<sub>2</sub>P, (c) FeNi LDHs, and (d) HP-Fe<sub>x</sub>Ni<sub>2-x</sub>P electrocatalysts.



**Fig. 7.** Structure model and the schematic illustration of the OER pathway, and the free energy diagram of the OER process of (a, b) FeNiOOH, (c, d)  $Fe_xNi_{2-x}P$  and (e, f) FeNiOOH/ $Fe_xNi_{2-x}P$ .

amorphous layer is formed on the surface of  $Fe_xNi_{2-x}P$  particles after the OER [46]. The elemental mapping in HP- $Fe_xNi_{2-x}P$  reveals the existence of Fe, Ni, and P with uniform distribution. B is not present after OER (Fig. 4e). To prove the stability of the structure of the catalyst, the sample was characterized after the stability test, as shown in Fig. S11. The morphology and phase structure of the catalyst did not change after the stability test. In addition, ICP-OES was carried out to further verify that phosphide is stably incorporated in the catalyst and is not lost during the stability test (Table S2).

XPS was carried out to investigate the surface composition and

chemical states of HP- $Fe_xNi_{2-x}P$  after OER (Fig. 5). Fig. 5a–d shows the high resolution XPS spectra of each element after OER. The signal related to  $Ni^0$  was not observed in Fig. 5a, because the surface of the catalyst was oxidized, which might be the reason for the appearance of the amorphous layer in Fig. 4d. The two new peaks located at 856.8 and 874.1 eV can be assigned to  $Ni^{3+} 2p_{3/2}$  and  $Ni^{3+} 2p_{1/2}$ , indicating the formation of high valent Ni sites, such as NiOOH. The  $Fe^0$  was also oxidized after OER, as testified by the disappearance of the signal related to  $Fe^0$  (Fig. 5b). A similar trend was also found in the case of P (Fig. 5c): the peaks located at 132.5, 133.4, and 190.3 eV can be assigned to P-O,

and the peak corresponding to  $P^0$  disappeared after OER. It is also noteworthy that the signal from B was negligible after OER (Fig. 5c). In addition, the O peak has a negative shift after the OER reaction, indicating that FeNiOOH appeared on the surface of the catalyst (Fig. 5d) [58]. Then the sample was also characterized after the stability test to investigate any possible change after long term operations. As shown in Fig. S12, the valence states of Ni and Fe did not change, calling for a strong stability of the catalyst.

To further study the activation process of the catalyst, we performed *in situ* Raman to analyze the active phase and the active species. The Raman spectrum of control sample  $Ni(OH)_2$  is shown in Fig. 6a. At open-circuit voltage, a  $Ni^{II}$ -O vibration peak at  $466\text{ cm}^{-1}$  appeared, indicating the existence of  $Ni(OH)_2$ . When the voltage reached 1.5 V (vs. RHE), a pair of peaks at around  $477$  and  $552\text{ cm}^{-1}$  appeared, which are associated with the  $E_g$  bending and the  $A_{1g}$  stretching vibration modes of  $Ni^{III}$ -O in NiOOH [47,48,50,61]. After stopping the reaction for 1 h, the peak location of NiOOH did not change, indicating that this phase is stable. In Fig. 6b, the *in situ* Raman spectra of  $Ni_2P$  showed that under the applied voltage,  $Ni_2P$  on the surface was gradually oxidized to NiOOH. Fig. 6c shows the *in situ* Raman data of FeNi LDHs. At open-circuit voltage, the peaks related to both  $Ni(OH)_2$  ( $466$  and  $534\text{ cm}^{-1}$ ) and  $NiFe_2O_4$  ( $313$  and  $725\text{ cm}^{-1}$ ) were observed, which agreed with the XRD results in Fig. 1h. At increased voltage, the hydroxide phase gradually transformed into oxyhydroxide phase with the appearance of  $Ni^{III}$ -O vibration at  $477$  and  $552\text{ cm}^{-1}$ , which are associated with the  $E_g$  bending and the  $A_{1g}$  stretching vibration modes of  $Ni^{III}$ -O in FeNiOOH. However, the  $NiFe_2O_4$  phase kept intact even under highly negative voltage, demonstrating that these metal oxide impurities are hard to be further oxidized into OER active oxyhydroxide phase. The *in situ* Raman data of HP- $Fe_xNi_{2-x}P$  catalyst (Fig. 6d) shows the same trend as  $Ni_2P$ , but with a lower voltage for the oxyhydroxide phase transformation. These results, combined with the above-discussed HRTEM and XPS data after OER, indicate that the phosphide phase in HP- $Fe_xNi_{2-x}P$  facilitates the formation of the FeNiOOH. In addition, the  $NaBH_4$  pretreatment is critical for the formation of a high level of phosphide phase.

DFT simulations were conducted to understand the mechanism for promoted OER performance, as shown in Fig. 7 [40,62]. The structural model of FeNiOOH,  $Fe_xNi_{2-x}P$ , and FeNiOOH/ $Fe_xNi_{2-x}P$  and their schematic illustration of the OER pathway are shown in Fig. 7a,c,e. The Gibbs free energy for each step on the surface of FeNiOOH and FeNiOOH/ $Fe_xNi_{2-x}P$  was calculated, and the rate-determining step (RDS) was identified as the formation of  $*O$  (Fig. 7b,f). The FeNiOOH (0 1  $\bar{1}$  2) facet exhibits a high Gibbs free energy for RDS (2.21 eV), while the FeNiOOH/ $Fe_xNi_{2-x}P$  heterostructure has a relatively low energy barrier (1.86 eV), indicating that the interfacial interaction is beneficial for this step. The DOS of the FeNiOOH and FeNiOOH/ $Fe_xNi_{2-x}P$  are shown in Fig. S13. FeNiOOH/ $Fe_xNi_{2-x}P$  shows an enhanced DOS near the Fermi energy level, revealing that phosphorization can effectively enhance the electronic conductivity of the material [21,26,63], which is in agreement with the results of the EIS analysis. Therefore, the excellent OER catalytic performance of FeNiOOH/ $Fe_xNi_{2-x}P$  can also be attributed to the high electronic conductivity and the ability to boost the transformation from  $*OH$  to  $*O$ .

#### 4. Conclusion

In summary, we have presented a new and simple three-step methodology for the production of a highly efficient and stable OER catalyst: (i) hydrothermal deposition, (ii)  $NaBH_4$  pretreatment, and (iii) *in situ* phosphorization. The  $NaBH_4$  pretreatment effectively promotes phosphatization and leads to the successful fabrication of HP- $Fe_xNi_{2-x}P$ . After electrochemical activation, the catalyst exhibits a high OER activity, for which a series of contributions can be identified: the presence of the *in situ* formed FeNiOOH/HP- $Fe_xNi_{2-x}P$  interface, the high density of exposed active sites, and high conductivity, endowing FeNiOOH/HP-

$Fe_xNi_{2-x}P$  with a low overpotential of 208 mV at  $10\text{ mA cm}^{-2}$ , a small Tafel slope of  $30\text{ mV dec}^{-1}$ , and long-term stability over 200 h, which can be comparable to the state-of-the-art reported OER electrocatalysts. The experimental results match the outcomes from DFT calculations in terms of Gibbs free energy of the interface, compared to the single material, and of electric conductivity, thanks to the modified DOS in the bilayered structure. These results are critically important for the practical implementation of OER for water splitting, but can be of interest also for other electrocatalytic applications, where electrical conductivity, the density of active sites, and surface reconstruction determine the functionality of the catalyst.

#### CRedit authorship contribution statement

Chendong Kou carried out the whole experiment and wrote the paper. Jieshu Zhou, Haibin Wang carried out the DFT simulations. Jingrui Han, Mei Han conducted the characterizations and performed the analysis of the results. Alberto Vomiero, Yongchang Liu, Hongyan Liang guided the whole project and revised the paper.

#### Declaration of Competing Interest

The authors declare that they have no known competing financial interests or personal relationships that could have appeared to influence the work reported in this paper.

#### Data Availability

Data will be made available on request.

#### Acknowledgments

This work was supported by the National Natural Science Foundation of China (NSFC No. 51771132, 52204320). A.V. acknowledges the Kempe Foundation, the Knut & Alice Wallenberg Foundation, and the ÅFORSK Foundation for financial support.

#### Appendix A. Supporting information

Supplementary data associated with this article can be found in the online version at doi:10.1016/j.apcatb.2023.122598.

#### References

- [1] S. Pan, R. Li, Q. Zhang, C. Cui, M. Wang, B. Shi, P. Wang, C. Zhang, B. Zhang, Y. Zhao, X. Zhang, An over 20 % solar-to-hydrogen efficiency system comprising a self-reconstructed NiCoFe-based hydroxide nanosheet electrocatalyst and monolithic perovskite/silicon tandem solar cell, *J. Mater. Chem. A* 9 (2021) 14085–14092.
- [2] X. Wang, K. Yao, L. Liu, C. Liu, H. Liang, Enhancing hot electron generation and injection with plasmonic nanostructures, *J. Alloy. Compd.* 893 (2022), 162214.
- [3] Q. Xu, H. Jiang, Y. Li, D. Liang, Y. Hu, C. Li, In-situ enriching active sites on co-doped Fe-Co<sub>4</sub>N@N-C nanosheet array as air cathode for flexible rechargeable Zn-air batteries, *Appl. Catal. B* 256 (2019), 117893.
- [4] S. Liu, R. Wan, Z. Lin, Z. Liu, Y. Liu, Y. Tian, D.-D. Qin, Z. Tang, Probing the Co role in promoting the OER and Zn-air battery performance of NiFe-LDH: a combined experimental and theoretical study, *J. Mater. Chem. A* 10 (2022) 5244–5254.
- [5] N. Wang, R.K. Miao, G. Lee, A. Vomiero, D. Sinton, A.H. Ip, H. Liang, E.H. Sargent, Suppressing the liquid product crossover in electrochemical CO<sub>2</sub> reduction, *SmartMat* 2 (2021) 12–16.
- [6] K. Yao, Y. Xia, J. Li, N. Wang, J. Han, C. Gao, M. Han, G. Shen, Y. Liu, A. Seifitokaldani, X. Sun, H. Liang, Metal-organic framework derived copper catalysts for CO<sub>2</sub> to ethylene conversion, *J. Mater. Chem. A* 8 (2020) 11117–11123.
- [7] K. Yao, H. Wang, X. Yang, Y. Huang, C. Kou, T. Jing, S. Chen, Z. Wang, Y. Liu, H. Liang, Metal-organic framework derived dual-metal sites for electroreduction of carbon dioxide to HCOOH, *Appl. Catal. B* 311 (2022), 121377.
- [8] L.-A. Stern, L. Feng, F. Song, X. Hu, Ni<sub>2</sub>P as a Janus catalyst for water splitting: the oxygen evolution activity of Ni<sub>2</sub>P nanoparticles, *Energy Environ. Sci.* 8 (2015) 2347–2351.
- [9] L. Yu, L. Wu, B. McElhenny, S. Song, D. Luo, F. Zhang, Y. Yu, S. Chen, Z. Ren, Ultrafast room-temperature synthesis of porous S-doped Ni/Fe (oxy)hydroxide



- electrodes for oxygen evolution catalysis in seawater splitting, *Energy Environ. Sci.* 13 (2020) 3439–3446.
- [10] D. Li, C. Liu, W. Ma, S. Xu, Y. Lu, W. Wei, J. Zhu, D. Jiang, Fe-doped NiCoP/Prussian blue analog hollow nanocubes as an efficient electrocatalyst for oxygen evolution reaction, *Electrochim. Acta* 367 (2021), 137492.
  - [11] Y. Qi, Q. Zhang, S. Meng, D. Li, W. Wei, D. Jiang, M. Chen, Iron-doped nickel cobalt ternary phosphide hyperbranched hierarchical arrays for efficient overall water splitting, *Electrochim. Acta* 334 (2020), 135633.
  - [12] P. Zhai, Y. Zhang, Y. Wu, J. Gao, B. Zhang, S. Cao, Y. Zhang, Z. Li, L. Sun, J. Hou, Engineering active sites on hierarchical transition bimetal oxides/sulfides heterostructure array enabling robust overall water splitting, *Nat. Commun.* 11 (2020) 5462.
  - [13] S. Yuan, J. Peng, B. Cai, Z. Huang, A.T. Garcia-Esparza, D. Sokaras, Y. Zhang, L. Giordano, K. Akkijaru, Y.G. Zhu, R. Hübner, X. Zou, Y. Román-Leshkov, Y. Shao-Horn, Tunable metal hydroxide-organic frameworks for catalysing oxygen evolution, *Nat. Mater.* 21 (2022) 673–680.
  - [14] K. Zhang, R. Zou, Advanced transition metal-based OER electrocatalysts: current status, opportunities, and challenges, *Small* 17 (2021), 2100129.
  - [15] M. Gong, Y. Li, H. Wang, Y. Liang, J.Z. Wu, J. Zhou, J. Wang, T. Regier, F. Wei, H. Dai, An advanced Ni-Fe layered double hydroxide electrocatalyst for water oxidation, *J. Am. Chem. Soc.* 135 (2013) 8452–8455.
  - [16] Z. Cai, X. Bu, P. Wang, J.C. Ho, J. Yang, X. Wang, Recent advances in layered double hydroxide electrocatalysts for the oxygen evolution reaction, *J. Mater. Chem. A* 7 (2019) 5069–5089.
  - [17] M. Ramadoss, Y. Chen, X. Chen, Z. Su, M. Karpuraranjith, D. Yang, M.A. Pandit, K. Muralidharan, Iron-modulated three-dimensional CoNiP vertical nanoarrays: an exploratory binder-free bifunctional electrocatalyst for efficient overall water splitting, *J. Phys. Chem. C* 125 (2021) 20972–20979.
  - [18] M. Ramadoss, Y. Chen, Y. Hu, W. Li, B. Wang, X. Zhang, X. Wang, B. Yu, Three-dimensional Ni/Ni<sub>3</sub>Fe embedded boron-doped carbon nanotubes nanochain frameworks as highly efficient and durable electrocatalyst for oxygen evolution reaction, *J. Power Sources* 451 (2020), 227753.
  - [19] M. Ramadoss, Y. Chen, Y. Hu, D. Yang, Three-dimensional porous nanoarchitecture constructed by ultrathin NiCoBO<sub>x</sub> nanosheets as a highly efficient and durable electrocatalyst for oxygen evolution reaction, *Electrochim. Acta* 321 (2019), 134666.
  - [20] X. Luo, P. Ji, P. Wang, R. Cheng, D. Chen, C. Lin, J. Zhang, J. He, Z. Shi, N. Li, S. Xiao, S. Mu, Interface engineering of hierarchical branched Mo-doped Ni<sub>3</sub>S<sub>2</sub>/Ni<sub>x</sub>P<sub>y</sub> hollow heterostructure nanorods for efficient overall water splitting, *Adv. Energy Mater.* 10 (2020), 1903891.
  - [21] N. Li, J. Han, K. Yao, M. Han, Z. Wang, Y. Liu, L. Liu, H. Liang, Synergistic phosphorized NiFeCo and MXene interaction inspired the formation of high-valence metal sites for efficient oxygen evolution, *J. Mater. Sci. Technol.* 106 (2022) 90–97.
  - [22] X. Zhang, Y. Li, Z. Wu, H. Sheng, Y. Hu, C. Li, H. Li, L. Cao, B. Dong, Crystalline/amorphous composite interface induced by NaBH<sub>4</sub> hydrolysis reaction: a new interfacial electrocatalyst for efficient oxygen evolution reaction, *Mater. Today Energy* 26 (2022), 100987.
  - [23] Y. Shi, M. Li, Y. Yu, B. Zhang, Recent advances in nanostructured transition metal phosphides: synthesis and energy-related applications, *Energy Environ. Sci.* 13 (2020) 4564–4582.
  - [24] H. Ren, X. Sun, C. Du, J. Zhao, D. Liu, W. Fang, S. Kumar, R. Chua, S. Meng, P. Kidkhunthod, L. Song, S. Li, S. Madhavi, Q. Yan, Amorphous Fe-Ni-P-B-O nanocages as efficient electrocatalysts for oxygen evolution reaction, *ACS Nano* 13 (2019) 12969–12979.
  - [25] J. Guo, Z. Zhan, T. Lei, P. Yin, Self-supported FeNiP nanosheet arrays as a robust bifunctional electrocatalyst for water splitting, *ACS Appl. Energy Mater.* 5 (2022) 5855–5866.
  - [26] J. Chen, Q. Long, K. Xiao, T. Ouyang, N. Li, S. Ye, Z.-Q. Liu, Vertically-interlaced NiFeP/MXene electrocatalyst with tunable electronic structure for high-efficiency oxygen evolution reaction, *Sci. Bull.* 66 (2021) 1063–1072.
  - [27] Y. Wu, C. Sun, H. Wang, S. Ji, B.G. Pollet, J. Lu, X. Tian, H. Liang, X. Wang, R. Wang, Ni<sub>2</sub>P nanoparticles-inserted NiFeP nanosheets with rich interfaces as efficient catalysts for the oxygen evolution reaction, *J. Alloy. Compd.* 903 (2022), 163855.
  - [28] X. Wang, J. Liu, Y. Hu, R. Ma, J. Wang, Oxygen vacancy-expedited ion diffusivity in transition-metal oxides for high-performance lithium-ion batteries, *Sci. China Mater.* 65 (2022) 1421–1430.
  - [29] L. Li, T. Meng, J. Wang, B. Mao, J. Huang, M. Cao, Oxygen vacancies boosting lithium-ion diffusion kinetics of lithium germanate for high-performance lithium storage, *ACS Appl. Mater. Interfaces* 13 (2021) 24804–24813.
  - [30] X. Wei, N. Li, X. Zhang, Co/CoO/C@B three-phase composite derived from ZIF67 modified with NaBH<sub>4</sub> solution as the electrocatalyst for efficient oxygen evolution, *Electrochim. Acta* 264 (2018) 36–45.
  - [31] L. Wu, L. Yu, Q. Zhu, B. McElhenny, F. Zhang, C. Wu, X. Xing, J. Bao, S. Chen, Z. Ren, Boron-modified cobalt iron layered double hydroxides for high efficiency seawater oxidation, *Nano Energy* 83 (2021), 105838.
  - [32] Y. Wang, S. Tao, H. Lin, S. Han, W. Zhong, Y. Xie, J. Hu, S. Yang, NaBH<sub>4</sub> induces a high ratio of Ni<sup>3+</sup>/Ni<sup>2+</sup> boosting OER activity of the NiFe LDH electrocatalyst, *RSC Adv.* 10 (2020) 33475–33482.
  - [33] Y. Wang, T. Zhou, K. Jiang, P. Da, Z. Peng, J. Tang, B. Kong, W.-B. Cai, Z. Yang, G. Zheng, Reduced mesoporous Co<sub>3</sub>O<sub>4</sub> nanowires as efficient water oxidation electrocatalysts and supercapacitor electrodes, *Adv. Energy Mater.* 4 (2014), 1400696.
  - [34] X. Ji, C. Cheng, Z. Zang, L. Li, X. Li, Y. Cheng, X. Yang, X. Yu, Z. Lu, X. Zhang, H. Liu, Ultrathin and porous δ-FeOOH modified Ni<sub>3</sub>S<sub>2</sub> 3D heterostructure nanosheets with excellent alkaline overall water splitting performance, *J. Mater. Chem. A* 8 (2020) 21199–21207.
  - [35] O. Gharbi, M.T.T. Tran, B. Tribollet, M. Turmine, V. Vivier, Revisiting cyclic voltammetry and electrochemical impedance spectroscopy analysis for capacitance measurements, *Electrochim. Acta* 343 (2020), 136109.
  - [36] M. Han, N. Wang, B. Zhang, Y. Xia, J. Li, J. Han, K. Yao, C. Gao, C. He, Y. Liu, Z. Wang, A. Seifitokaldani, X. Sun, H. Liang, High-valent nickel promoted by atomically embedded copper for efficient water oxidation, *ACS Catal.* 10 (2020) 9725–9734.
  - [37] G. Kresse, J. Furthmüller, Efficient iterative schemes for ab initio total-energy calculations using a plane-wave basis set, *Phys. Rev. B* 54 (1996) 11169–11186.
  - [38] J.P. Perdew, K. Burke, M. Ernzerhof, Generalized gradient approximation made simple, *Phys. Rev. Lett.* 80 (1998) (891–891).
  - [39] H. Xu, D. Cheng, D. Cao, X.C. Zeng, A universal principle for a rational design of single-atom electrocatalysts, *Nat. Catal.* 1 (2018) 339–348.
  - [40] L.-F. Li, Y.-F. Li, Z.-P. Liu, Oxygen evolution activity on NiOOH catalysts: four-coordinated Ni cation as the active site and the hydroperoxide mechanism, *ACS Catal.* 10 (2020) 2581–2590.
  - [41] S. Grimme, Semiempirical GGA-type density functional constructed with a long-range dispersion correction, *J. Comput. Chem.* 27 (2006) 1787–1799.
  - [42] Y. Li, H. Zhang, M. Jiang, Q. Zhang, P. He, X. Sun, 3D self-supported Fe-doped Ni<sub>2</sub>P nanosheet arrays as bifunctional catalysts for overall water splitting, *Adv. Funct. Mater.* 27 (2017), 1702513.
  - [43] J. He, X. Zhou, P. Xu, J. Sun, Promoting electrocatalytic water oxidation through tungsten-modulated oxygen vacancies on hierarchical FeNi-layered double hydroxide, *Nano Energy* 80 (2021), 105540.
  - [44] L. Wu, L. Yu, F. Zhang, D. Wang, D. Luo, S. Song, C. Yuan, A. Karim, S. Chen, Z. Ren, Facile synthesis of nanoparticle-stacked tungsten-doped nickel iron layered double hydroxide nanosheets for boosting oxygen evolution reaction, *J. Mater. Chem. A* 8 (2020) 8096–8103.
  - [45] H. Yang, Y. Liu, S. Luo, Z. Zhao, X. Wang, Y. Luo, Z. Wang, J. Jin, J. Ma, Lateral-size-mediated efficient oxygen evolution reaction: insights into the atomically thin quantum dot structure of NiFe<sub>2</sub>O<sub>4</sub>, *ACS Catal.* 7 (2017) 5557–5567.
  - [46] B. Zhang, Y.H. Lui, H. Ni, S. Hu, Bimetallic (Fe<sub>2</sub>Ni<sub>1-x</sub>)<sub>2</sub>P nanoarrays as exceptionally efficient electrocatalysts for oxygen evolution in alkaline and neutral media, *Nano Energy* 38 (2017) 553–560.
  - [47] D.S. Hall, D.J. Lockwood, S. Poirier, C. Bock, B.R. MacDougall, Raman and infrared spectroscopy of  $\alpha$  and  $\beta$  phases of thin nickel hydroxide films electrochemically formed on nickel, *J. Phys. Chem. A* 116 (2012) 6771–6784.
  - [48] O. Diaz-Morales, D. Ferrus-Suspedra, M.T.M. Koper, The importance of nickel oxyhydroxide deprotonation on its activity towards electrochemical water oxidation, *Chem. Sci.* 7 (2016) 2639–2645.
  - [49] Y.J. Wu, J. Yang, T.X. Tu, W.Q. Li, P.F. Zhang, Y. Zhou, J.F. Li, J.T. Li, S.G. Sun, Evolution of cationic vacancy defects: a motif for surface restructuring of OER precatalyst, *Angew. Chem. Int. Ed.* 60 (2021) 26829–26836.
  - [50] L. Peng, N. Yang, Y. Yang, Q. Wang, X. Xie, D. Sun-Waterhouse, L. Shang, T. Zhang, G.I.N. Waterhouse, Atomic cation-vacancy engineering of nife-layered double hydroxides for improved activity and stability towards the oxygen evolution reaction, *Angew. Chem. Int. Ed.* 60 (2021) 24612–24619.
  - [51] A. Ahlawat, V.G. Sathe, Raman study of NiFe<sub>2</sub>O<sub>4</sub> nanoparticles, bulk and films: effect of laser power, *J. Raman Spectrosc.* 42 (2011) 1087–1094.
  - [52] H. Sun, X. Xu, Z. Yan, X. Chen, F. Cheng, P.S. Weiss, J. Chen, Porous multishelled Ni<sub>2</sub>P hollow microspheres as an active electrocatalyst for hydrogen and oxygen evolution, *Chem. Mater.* 29 (2017) 8539–8547.
  - [53] S.-F. Hung, Y. Zhu, G.-Q. Tzeng, H.-C. Chen, C.-S. Hsu, Y.-F. Liao, H. Ishii, N. Hiraoka, H.M. Chen, In situ spatially coherent identification of phosphide-based catalysts: crystallographic latching for highly efficient overall water electrolysis, *ACS Energy Lett.* 4 (2019) 2813–2820.
  - [54] L. Yu, Q. Zhu, S. Song, B. McElhenny, D. Wang, C. Wu, Z. Qin, J. Bao, Y. Yu, S. Chen, Z. Ren, Non-noble metal-nitride based electrocatalysts for high-performance alkaline seawater electrolysis, *Nat. Commun.* 10 (2019) 5106.
  - [55] D. Senthil Raja, H.-W. Lin, S.-Y. Lu, Synergistically well-mixed MOFs grown on nickel foam as highly efficient durable bifunctional electrocatalysts for overall water splitting at high current densities, *Nano Energy* 57 (2019) 1–13.
  - [56] Y. Chen, H. Yao, F. Kong, H. Tian, G. Meng, S. Wang, X. Mao, X. Cui, X. Hou, J. Shi, V<sub>2</sub>C MXene synergistically coupling FeNi LDH nanosheets for boosting oxygen evolution reaction, *Appl. Catal. B* 297 (2021), 120474.
  - [57] N. Wang, A. Xu, P. Ou, S.-F. Hung, A. Ozden, Y.-R. Lu, J. Abed, Z. Wang, Y. Yan, M.-J. Sun, Y. Xia, M. Han, J. Han, K. Yao, F.-Y. Wu, P.-H. Chen, A. Vomiero, A. Seifitokaldani, X. Sun, D. Sinton, Y. Liu, E.H. Sargent, H. Liang, Boride-derived oxygen-evolution catalysts, *Nat. Commun.* 12 (2021) 6089.
  - [58] J. Masa, I. Sinev, H. Mistry, E. Ventosa, M. de la Mata, J. Arbiol, M. Muhler, B. Roldan Cuenya, W. Schuhmann, Ultrathin high surface area nickel boride (Ni<sub>3</sub>B) nanosheets as highly efficient electrocatalyst for oxygen evolution, *Adv. Energy Mater.* 7 (2017), 1700381.
  - [59] H. Roh, H. Jung, H. Choi, J.W. Han, T. Park, S. Kim, K. Yong, Various metal (Fe, Mo, V, Co)-doped Ni<sub>2</sub>P nanowire arrays as overall water splitting electrocatalysts and their applications in unassisted solar hydrogen production with STH 14 %, *Appl. Catal. B* 297 (2021), 120434.
  - [60] J. Wang, X. Ma, F. Qu, A.M. Asiri, X. Sun, Fe-doped Ni<sub>2</sub>P nanosheet array for high-efficiency electrochemical water oxidation, *Inorg. Chem.* 56 (2017) 1041–1044.

- [61] M.W. Louie, A.T. Bell, An investigation of thin-film Ni–Fe oxide catalysts for the electrochemical evolution of oxygen, *J. Am. Chem. Soc.* 135 (2013) 12329–12337.
- [62] D. Friebe, M.W. Louie, M. Bajdich, K.E. Sanwald, Y. Cai, A.M. Wise, M.J. Cheng, D. Sokaras, T.C. Weng, R. Alonso-Mori, R.C. Davis, J.R. Bargar, J.K. Nørskov, A. Nilsson, A.T. Bell, Identification of highly active Fe sites in (Ni,Fe)OOH for electrocatalytic water splitting, *J. Am. Chem. Soc.* 137 (2015) 1305–1313.
- [63] B. Fei, Z. Chen, J. Liu, H. Xu, X. Yan, H. Qing, M. Chen, R. Wu, Ultrathinning nickel sulfide with modulated electron density for efficient water splitting, *Adv. Energy Mater.* 10 (2020), 2001963.